ACT/FHS SYSTEM IDENTIFICATION INCLUDING ENGINE TORQUE AND MAIN ROTOR SPEED USING THE PBSIDOPT METHOD

Johannes Wartmann
Johannes.Wartmann@dlr.de
DLR (German Aerospace Center), Institute of Flight Systems
Lilienthalplatz 7, 38108 Braunschweig, Germany

ABSTRACT

The identified models of DLR's research rotorcraft ACT/FHS have been improved constantly over the last years. Nevertheless, the current models still have deficits that are attributed to missing engine dynamics. Therefore, in this paper the influence of engine torque and main rotor speed on model fidelity and model structure is investigated by identifying two linear models of the ACT/FHS. The first model's dynamics and outputs are identified using the rigid body states, engine torque and main rotor speed. The dynamics of the second model are identified using only the rigid body states. This model includes torque and rotor speed only as additional outputs that are not weighted during the identification of the model's dynamics. To avoid the definition of a model structure beforehand, the optimized predictor-based subspace identification method is used as system identification method with dedicated flight test data of the ACT/FHS. The results of this paper are used to clarify if torque and rotor speed are necessary for high fidelity system identification using other identification methods. Furthermore, the experimental setup, the PBSIDopt method and the model selection process are described briefly.

NOMENCLATURE

A, B, C, D	discrete time state space matrices
$A_\mathrm{ct}, B_\mathrm{ct}, C_\mathrm{ct}$	continuous time state space matrices
A_K, B_K	predictor form state space matrices
E, U, X, Y	data matrices for system innovations, inputs, states and outputs (with indexes)
e_k, u_k, x_k, y_k	discrete time innovation, input, state and output vectors at k-th time step
f, p	future and past window length
G_1	model including rigid body, torque and rotor speed dynamics (and outputs)
G_2	model including rigid body dynamics, torque and rotor speed as outputs only
J_RMS	root mean square error of rigid body model outputs
$J_{Q,\mathrm{RMS}}$	root mean square error of engine torque
$J_{\Omega,\mathrm{RMS}}$	root mean square error of rotor speed
K	Kalman gain matrix
N	number of measurements
n	model order
n_u, n_y	number of inputs and number of outputs
p, q, r	roll, pitch and yaw rates
Q	engine torque
S	diagonal matrix with singular values
T	transformation matrix
u, v, w	airspeed components (aircraft fixed)
y_m	measured output (index m)
z_k	merged input-output vector at k-th time step
Z	data matrices for merged input-outputs (with indexes)
δ_x, δ_y	longitudinal and lateral cyclic pilot controls
δ_p, δ_0	pedal and collective pilot controls
ϕ, θ	roll and pitch attitude angles
$\mathscr{K}$	extended controllability matrix
Γ	extended observability matrix
Ω	main rotor speed
ω	angular frequency
ACT/FHS	Active Control Technology / Flying Helicopter Simulator
ARX	AutoRegressive model with eXogenous input
PBSIDopt	optimized predictor-based subspace identification (method)
RMS	root mean square (error)

1. INTRODUCTION

Most rotorcraft system identification approaches use frequency domain methods to determine linear models for the helicopter dynamics. Depending on the complexity of the model and whether rotor and/or engine states are included, the identified models can be accurate for frequencies up to 30 rad/s [1]. The identification of such complex models and the associated flight tests are laborious tasks, but essential to gain useful models for system analysis, simulation and flight control development.

Within the DLR project ALLFlight (Assisted Low Level Flight and Landing on Unprepared Landing Sites, [2, 3]) models of DLR's research helicopter EC135 ACT/FHS (Active Control Technology/Flying Helicopter Simulator) have been identified using a Maximum Likelihood frequency domain method [4, 5]. The identified models are physically motivated, i.e. the models consist of states for the rigid body motion, implicit rotor flapping, inflow and regressive lead-lag dynamics. The corresponding model structure has to be predefined for the system identification step and has been adjusted several times to enhance the estimated models [6, 7]. Thus, the Maximum Likelihood method is mainly a parameter estimation approach. In the last years, these models have been analyzed and used for flight control and simulation purposes at DLR [8–10]. Nonetheless, the current models of the ACT/FHS have deficits that are attributed to missing engine dynamics.

Today, state of the art time domain system identification methods like the optimized predictor-based subspace identification method (PBSIDopt) offer the possibility to estimate high order models for multiple input and output systems without having to define a model structure beforehand [11, 12]. Since the results of the PBSIDopt method seem to be suitable for rotorcraft system identification [13–15], the method has been applied to flight test data of the ACT/FHS research rotorcraft in a preliminary evaluation in [16]. The identified model showed a high accuracy over a broad frequency range even for off-axis coupling.

Based on this preliminary evaluation, two different models of the ACT/FHS research rotorcraft are identified in this paper to investigate the contribution of engine torque and main rotor speed to the model fidelity and the model structure. The first model's dynamics and outputs rely on the rigid body states as well as the engine torque and main rotor speed. The second model uses the rigid body states in the identification step, but includes torque and rotor speed only as additional outputs. Thus, the dynamics of the second model are based solely on rigid body states and just contain engine torque and main rotor speed outputs for the comparison with the first model. Both models are identified using the PBSIDopt method in the time domain with flight test data of the ACT/FHS at 90 knots forward flight.

In this paper, the experimental setup including flight path reconstruction and data processing steps are first described in detail. The applied PBSIDopt method is covered subsequently and the different identification approaches for both models are characterized. Next, the models with and without accounting for engine torque and rotor speed are determined. Then, the identified models are compared with respect to model fidelity, structure and complexity. The answer to what extent the overall model fidelity is dependent on the engine torque and main rotor speed is answered. The results are discussed and summarized at the end of this paper.

2. EXPERIMENTAL SETUP

2.1. The ACT/FHS Research Rotorcraft

The ACT/FHS, depicted in Figure 1, is the main testbed for rotorcraft research at DLR [17]. It is a highly modified Eurocopter EC135, a twin-engine helicopter with fenestron and bearingless main rotor and a maximum takeoff weight of about 2.9 t.

Figure 1: DLR's research rotorcraft ACT/FHS

The mechanical controls of this testbed have been replaced by a full-authority fly-by-wire/fly-by-light control system to apply control inputs generated by an experimental system to the ACT/FHS in flight. Thus, the dynamics of the ACT/FHS are not comparable to data from a production EC135 rotorcraft. The ACT/FHS is equipped with various sensors, e.g. a noseboom, two differential GPS receivers, a flight test instrumentation measuring the main rotor speed etc. and a rotor data acquisition system providing the main rotor shaft torsion moment. For the investigations in this paper, the main rotor shaft torque is used as a substitute for the engine torque since it is not filtered. The shaft torque is scaled to fit the engine torque. System identification of the ACT/FHS yields the necessary models for the model-based control and in-flight simulation research activities at DLR.

2.2. Flight Test Data

Dedicated flight tests with the ACT/FHS research rotorcraft for system identification and model validation have been conducted in 2009 and 2010. These flight tests consist of at least two manual frequency sweeps with increasing frequency up to about 2 Hz for each control input at each of five reference airspeeds, i.e. hover, 30, 60, 90 and 120 knots. During the manual frequency sweeps, a flight state near the reference trim condition has been maintained by applying uncorrelated, pulse-type inputs on the secondary controls only. In this way, cross-correlations between the four control inputs are minimized. At the same flight conditions, computer generated 3-2-1-1 multistep input maneuvers have

been recorded as a dissimilar basis for model validation purposes.

For this paper, eight manual frequency sweeps at 90 knots have been selected from the system identification database. Furthermore, eight 3-2-1-1 multistep maneuvers at the same airspeed have been chosen for model validation. The selected maneuvers, the applied control amplitudes and the test durations are summarized in Table 1.

maneuver	axis	amplitude	duration
2x manual sweep	δ_x	max. 10 %	134 s
2x manual sweep	δ_y	max. 12 %	146 s
2x manual sweep	δ_p	max. 13 %	131 s
2x manual sweep	δ_0	max. 8 %	133 s
2x automatic 3-2-1-1	δ_x	±2 %	9 s
2x automatic 3-2-1-1	δ_y	±4 %	9 s
2x automatic 3-2-1-1	δ_p	±8 %	9 s
2x automatic 3-2-1-1	δ_0	±4 %	9 s

Table 1: Used maneuvers for ACT/FHS system identification and model validation at 90 knots forward flight

The rotorcraft inputs and outputs used for system identification are available with a sampling time of 8 ms. Thus, the manual sweep maneuvers consist of around 17.000 data points per channel. For comparison in the frequency domain, frequency response functions for the ACT/FHS have been generated from the manual frequency sweep data.

2.3. Flight Path Reconstruction and Data Pre-Processing

It is common practice to use the motion of the rotorcraft's center of gravity for rotorcraft system identification and model validation. The corresponding rotorcraft states cannot be measured directly, since the installed sensors are not in the center of gravity and do not provide all necessary data. Furthermore, rotorcraft system identification is performed using the helicopter's motion with respect to the surrounding air. Thus, these states have to be estimated or calculated from the measured data. At DLR, a flight path reconstruction is used to estimate the motion of the rotorcraft's center of gravity and the motion of the local wind from raw sensor data after flight.

Since the flight path reconstruction is performed post-flight, two Unscented Kalman Filters are used to estimate the rotatory and translatory states of the rotorcraft. The first filter corrects the alignment of all rotatory measurements and then estimates the rotatory rotorcraft states including the angular accelerations. The rotatory state estimates are then used to transform the translatory measurements to the center of gravity. Subsequently, the measurements of the air data systems (i.e. the true airspeed), of the noseboom (true airspeed, angle of attack and angle of sideslip) and the cor-

rected translatory measurements are fused in the second filter to estimate the motion of the center of gravity and of the surrounding air. Both Unscented Kalman Filters and the used sensors are described in detail in [18].

In addition to [18], the estimated states are processed by two separate Unscented Rauch-Tung-Striebel Smoothers described in [19]. Using this method, the estimated states are smoothed in an optimal sense without an additional phase delay. Measured signals that are not included in the flight path reconstruction (like the helicopter controls, the engine torque and main rotor speed) are filtered by a zero-phase low-pass filter with a cutoff frequency of 12.5 Hz. As mentioned before, the estimated rotorcraft states and the filtered measurements are available with a sampling time of 8 ms.

3. SYSTEM IDENTIFICATION

3.1. The PBSIDopt Method

A discrete linear time invariant state space model in innovation form is given by

$$(1a) \qquad \boldsymbol{x}_{k+1} = \boldsymbol{A}\boldsymbol{x}_k + \boldsymbol{B}\boldsymbol{u}_k + \boldsymbol{K}\boldsymbol{e}_k$$
$$(1b) \qquad \boldsymbol{y}_k = \boldsymbol{C}\boldsymbol{x}_k + \boldsymbol{D}\boldsymbol{u}_k + \boldsymbol{e}_k$$

with the system inputs $\boldsymbol{u}_k \in \mathbb{R}^{n_u}$, outputs $\boldsymbol{y}_k \in \mathbb{R}^{n_y}$ and states $\boldsymbol{x}_k \in \mathbb{R}^n$. The zero-mean system innovations $\boldsymbol{e}_k \in \mathbb{R}^{n_y}$ are assumed to be white process noise. A finite set of data points $\boldsymbol{u}_k$ and $\boldsymbol{y}_k$ with $k = 1 \ldots N$ is considered for system identification using the PBSIDopt method.

Assuming there is no direct feedthrough $\boldsymbol{D} = \boldsymbol{0}$, the system equations (1) are transformed into the predictor form

$$(2a) \qquad \boldsymbol{x}_{k+1} = \boldsymbol{A}_K \boldsymbol{x}_k + \boldsymbol{B}_K \boldsymbol{z}_k$$
$$(2b) \qquad \boldsymbol{y}_k = \boldsymbol{C}\boldsymbol{x}_k + \boldsymbol{e}_k$$

with $\boldsymbol{A}_K = \boldsymbol{A} - \boldsymbol{K}\boldsymbol{C}$, $\boldsymbol{B}_K = (\boldsymbol{B}\ \boldsymbol{K})$ and $\boldsymbol{z}_k = (\boldsymbol{u}_k\ \boldsymbol{y}_k)^T$.

Consequently, the $(k{+}p)$-th state $\boldsymbol{x}_{k+p}$ is determined by

$$(3)$$
$$\boldsymbol{x}_{k+p} = \boldsymbol{A}_K \boldsymbol{x}_{x+p-1} + \boldsymbol{B}_K \boldsymbol{z}_{x+p-1}$$
$$= \boldsymbol{A}_K^p \boldsymbol{x}_k + \begin{pmatrix} \boldsymbol{A}_K^{p-1}\boldsymbol{B}_K & \ldots & \boldsymbol{B}_K \end{pmatrix} \begin{pmatrix} \boldsymbol{z}_k \\ \vdots \\ \boldsymbol{z}_{k+p-1} \end{pmatrix}$$

and the $(k{+}p)$-th output $\boldsymbol{y}_{k+p}$ is calculated using

$$(4) \qquad \boldsymbol{y}_{k+p} = \boldsymbol{C}\boldsymbol{A}_K^p \boldsymbol{x}_k + \boldsymbol{C}\mathscr{K}^p \begin{pmatrix} \boldsymbol{z}_k \\ \vdots \\ \boldsymbol{z}_{k+p-1} \end{pmatrix}$$

with

(5) $$\mathscr{K}^p = \begin{pmatrix} \boldsymbol{A}_K^{p-1} \boldsymbol{B}_K & \ldots & \boldsymbol{B}_K \end{pmatrix}.$$

Assuming p (called the "past window length" hereafter) is large and $\boldsymbol{A}_K$ is stable, the term $\boldsymbol{A}_K^p$ in equations (3) and (4) can be neglected and the $(p+1)$-th to N-th system states and outputs are approximated by

(6a) $$\boldsymbol{X}_{p+1} \approx \mathscr{K}^p \boldsymbol{Z}_p$$

(6b) $$\boldsymbol{Y}_{p+1} \approx \boldsymbol{C} \mathscr{K}^p \boldsymbol{Z}_p + \boldsymbol{E}_{p+1}.$$

The output data matrix $\boldsymbol{Y}_{p+1}$ is given by

(7) $$\boldsymbol{Y}_{p+1} = \begin{pmatrix} \boldsymbol{y}_{p+1} & \boldsymbol{y}_{p+2} & \ldots & \boldsymbol{y}_N \end{pmatrix}.$$

The innovation data matrix $\boldsymbol{E}_{p+1}$ and the input data matrix $\boldsymbol{U}_p$ (used later in this section) are set up in the same manner. The merged input-output vectors $\boldsymbol{z}$ of the predictor form model are collected in the data matrix

(8) $$\boldsymbol{Z}_p = \begin{pmatrix} \boldsymbol{z}_1 & \boldsymbol{z}_2 & \ldots & \boldsymbol{z}_{N-p} \\ \boldsymbol{z}_2 & \boldsymbol{z}_3 & \ldots & \boldsymbol{z}_{N-p+1} \\ \vdots & \vdots & \ldots & \vdots \\ \boldsymbol{z}_p & \boldsymbol{z}_{p+1} & \ldots & \boldsymbol{z}_{N-1} \end{pmatrix}.$$

To reconstruct the system states in the first PBSIDopt calculation step, the following linear regression is solved

(9) $$\min_{\boldsymbol{C}\mathscr{K}^p} \|\boldsymbol{Y}_{p+1} - \boldsymbol{C}\mathscr{K}^p \boldsymbol{Z}_p\|.$$

The linear regression corresponds to the identification of an high order ARX model (AutoRegressive model with eXogenous input). Recalling the definition of $\mathscr{K}^p$ in equation (5), the estimate $\widetilde{\boldsymbol{C}\mathscr{K}^p}$ is used to set up the product of the extended observability matrix $\boldsymbol{\Gamma}^f$ and the extended controllability matrix $\mathscr{K}^p$

(10) $$\boldsymbol{\Gamma}^f \mathscr{K}^p = \begin{pmatrix} \boldsymbol{C}\boldsymbol{A}_K^{p-1}\boldsymbol{B}_K & \ldots & \boldsymbol{C}\boldsymbol{B}_K \\ \boldsymbol{0} & \ldots & \boldsymbol{C}\boldsymbol{A}_K\boldsymbol{B}_K \\ \vdots & \vdots & \vdots \\ \boldsymbol{0} & \ldots & \boldsymbol{C}\boldsymbol{A}_K^{f-1}\boldsymbol{B}_K \end{pmatrix}$$

with the future window length f.

Since

(11) $$\boldsymbol{\Gamma}^f \boldsymbol{X}_{p+1} \approx \boldsymbol{\Gamma}^f \mathscr{K}^p \boldsymbol{Z}_p,$$

the singular value decomposition (SVD)
(12)
$$\boldsymbol{\Gamma}^f \mathscr{K}^p \boldsymbol{Z}_p = \boldsymbol{U}\boldsymbol{S}\boldsymbol{V}^T = \begin{pmatrix} \boldsymbol{U}_n & \tilde{\boldsymbol{U}} \end{pmatrix} \begin{pmatrix} \boldsymbol{S}_n & \boldsymbol{0} \\ \boldsymbol{0} & \tilde{\boldsymbol{S}} \end{pmatrix} \begin{pmatrix} \boldsymbol{V}_n^T \\ \tilde{\boldsymbol{V}}^T \end{pmatrix}$$

is applied to reconstruct the system states $\boldsymbol{X}_{p+1}$

(13) $$\boldsymbol{X}_{p+1} \approx \boldsymbol{S}_n^{\frac{1}{2}} \boldsymbol{V}_n^T.$$

The choice of n determines the resulting model order since only the n largest singular values $\boldsymbol{S}_n$ are used to reconstruct the system state sequence $\boldsymbol{X}_{p+1}$. An analysis of the singular values in $\boldsymbol{S}$ can be used to select an appropriate model order n. Alternatively, a high order model can be identified at this stage and other model order reduction techniques can be used afterwards to arrive at models with lower order.

In the second step, the system matrices of $\boldsymbol{A}$, $\boldsymbol{B}$ and $\boldsymbol{C}$ from equation (1) are determined from the reconstructed states $\boldsymbol{X}_{p+1}$ and the data matrices $\boldsymbol{Y}_{p+1}$ and $\boldsymbol{U}_p$ via

(14a) $$\min_{\boldsymbol{C}} \|\boldsymbol{Y}_{p+1} - \boldsymbol{C}\boldsymbol{X}_{p+1}\|$$

(14b) $$\min_{\boldsymbol{A},\boldsymbol{B}} \|\boldsymbol{X}_{k+1} - \boldsymbol{A}\boldsymbol{X}_k - \boldsymbol{B}\boldsymbol{U}_p\|$$

with $\boldsymbol{X}_{k+1} = \boldsymbol{X}_{p+1}(:, 2{:}N)$ and $\boldsymbol{X}_k = \boldsymbol{X}_{p+1}(:, 1{:}N\text{-}1)$ (in MATLAB notation). The inverse bilinear (or any other discrete time to continuous time transformation) can then be applied to calculate the continuous time state space model

(15a) $$\dot{\boldsymbol{x}} = \boldsymbol{A}_{\mathrm{ct}}\boldsymbol{x} + \boldsymbol{B}_{\mathrm{ct}}\boldsymbol{u}$$

(15b) $$\boldsymbol{y} = \boldsymbol{C}_{\mathrm{ct}}\boldsymbol{x}.$$

Since eight sweeps are used for the system identification of the ACT/FHS, see section 2.2, all data matrices have to be adjusted to consider all maneuvers in one calculation step. For j datasets the output data matrix is given by

(16) $$\boldsymbol{Y}_{p+1} = \begin{pmatrix} \boldsymbol{Y}_{p+1,1} & \ldots & \boldsymbol{Y}_{p+1,j} \end{pmatrix}.$$

The other data matrices are extended to multiple maneuvers in the same way.

In summary, the computational steps of the PBSIDopt algorithm are:

1. Set up the matrices $\boldsymbol{Y}_{p+1}$ and $\boldsymbol{Z}_p$ from equation (16) or equation (7) and (8) respectively,
2. Solve the least squares problem from equation (9),
3. Set up $\boldsymbol{\Gamma}^f \mathscr{K}^p$ from equation (10),
4. Solve the SVD from equation (12),
5. Calculate an estimate of $\boldsymbol{X}_{p+1}$ from equation (13),
6. Solve the least squares problems from equation (14).

3.2. Separate Identification of Model Dynamics and Output Equations

Most system identification approaches minimize a cost function based on the difference between measured and simulated outputs in the time or frequency domain. In general, the model outputs are model states at the same time. Further model outputs are often used to improve the estimation of selected model parameters.

The PBSIDopt algorithm is not comparable to these types of system identification approaches, since it estimates a high

order ARX model to reconstruct the system states X_{p+1} in the first step. As only the observable and controllable model subspace of the given system inputs and outputs can be identified, the inputs and outputs used in this step determine the system dynamics. Consequently, the corresponding system matrices A and B (that are determined in the second calculation step) can only reproduce the system dynamics covered in the first step.

In this paper, this relationship is used to analyze the influence of specific outputs (namely engine torque and main rotor speed) on the whole model. Therefore, two different models are estimated with the following approach:

1. Model G_1 uses all outputs y_k (rigid body states, torque and rotor speed, see the definition below) for the reconstruction of system states and the estimation of the system matrices A, B and C afterward,
2. Model G_2 uses solely a subset $\widetilde{y}_k$ of all outputs (namely the rigid body states) for the reconstruction of the system states and consequently for the estimation of A and B, but uses all outputs y_k for the estimation of the output matrix C.

Thus, the dynamics and the outputs of model G_1 rely on all measured outputs y_k. The dynamics of model G_2 are based merely on the given output subset $\widetilde{y}_k$. Nevertheless, G_2 has the same outputs as G_1 for comparison, but these additional outputs are not weighted during the identification of the model's dynamics. The differences of both models system identification approaches are depicted in Figure 2.
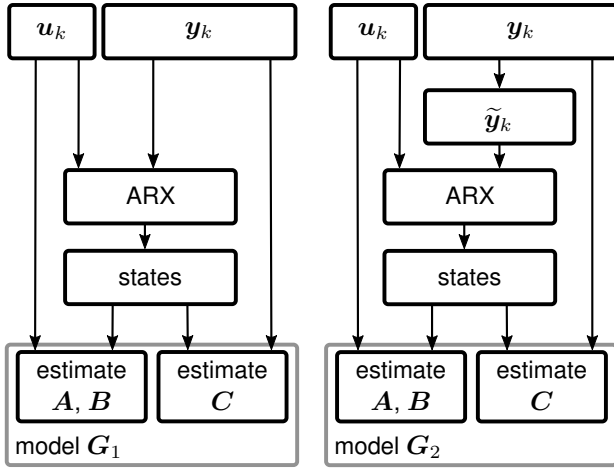

Figure 2: System identification approaches and used data for model G_1 and G_2

The two models G_1 and G_2 of the ACT/FHS are identified using the processed manual frequency sweeps described in the sections 2.2 and 2.3. The 3-2-1-1 multistep inputs are then used for model validation. Both models use the longitudinal cyclic control δ_x, lateral cyclic δ_y, pedal δ_p and collective δ_0 as inputs u_k

$$(17) \qquad u_k = \begin{pmatrix} \delta_x & \delta_y & \delta_p & \delta_0 \end{pmatrix}^T .$$

The whole output dataset y_k for model G_1 consists of the helicopter velocity components u, v and w, the angular rates p, q and r, the attitude angles ϕ and θ, the engine torque Q and the main rotor speed Ω

$$(18) \quad y_k = \begin{pmatrix} u & v & w & p & q & r & \phi & \theta & Q & \Omega \end{pmatrix}^T .$$

The output subset $\widetilde{y}_k$ used for the ARX model identification of G_2 and the corresponding system state reconstruction is set up by the rigid body motion states of the ACT/FHS only

$$(19) \qquad \widetilde{y}_k = \begin{pmatrix} u & v & w & p & q & r & \phi & \theta \end{pmatrix}^T .$$

In summary, model G_1 is identified using the whole output dataset for the estimation of its dynamics and outputs. The dynamics of model G_2 are estimated using only the rigid body states, but not the engine torque Q and the main rotor speed Ω. Thus, the system dynamics of G_2 are based on the rigid body states only and do not include the engine torque and rotor speed. To make the models comparable, the output matrix C in equation (14a) is estimated using the full outputs y_k and consequently, the resulting model G_2 has the same outputs as model G_1.

3.3. ACT/FHS Model Selection

For the PBSIDopt method, it is required to select the parameters past window length p, future window length f and model order n. These parameters have a significant influence on the resulting model accuracy and should be chosen according to the guidelines given in [11] and [12]. The selection of an optimal future window length f is particularly time consuming as f highly depends on the used input signals and other experiment conditions. The minimization of the identified model's asymptotic variance is proposed in [12] to select the optimal f. Furthermore, the past window length p should be larger than the model order n and large enough to satisfy $A_K^p \approx 0$.

In this paper, $p = 50$ is selected as a minimum past window length for system identification. Starting from this precondition, a parameter study is used to select the best model identified for every suitable parameter setting. Accordingly, over 13,000 models of G_1 and G_2 are identified varying the parameters p, f and n in the following ranges:

$$(20a) \qquad p_{i_p} = \begin{pmatrix} 50 & 60 \ldots 100 & 125 \ldots 250 \end{pmatrix}$$

$$(20b) \qquad f_{i_f} = \begin{pmatrix} 1 & 5 & 10 \ldots 20 & 30 \ldots 100 \end{pmatrix}$$

$$(20c) \qquad n_{i_n} = \begin{pmatrix} 8 & 9 \ldots 120 \end{pmatrix} .$$

To compare the model accuracies, each identified model is validated in the time domain using the model validation maneuvers described before. Initial states x_0 and output

offsets $\boldsymbol{y}_0$ are optimized for every model and maneuver set to minimize the difference between the measurements $\boldsymbol{y}_\mathrm{m}$ and the simulated model outputs $\boldsymbol{y}$. The root mean square (RMS) error J_RMS between $\boldsymbol{y}_\mathrm{m}$ and $\boldsymbol{y}$ is chosen as a measure for model accuracy

$$(21) \quad J_\mathrm{RMS} = \sqrt{\frac{1}{n_y N} \sum_{k=1}^{N} (\boldsymbol{y}_{\mathrm{m},k} - \boldsymbol{y}_k)^T (\boldsymbol{y}_{\mathrm{m},k} - \boldsymbol{y}_k)} \ .$$

According to [1], the model accuracy can be considered as good for RMS errors between

$$(22) \qquad\qquad J_\mathrm{RMS} \leq 1.0 \text{ to } 2.0$$

for coupled helicopter models validated in the time domain, if the velocities are scaled to ft/s, rates to deg/s and attitudes to deg. In J_RMS only the RMS errors of the rigid body states u, v, w, p, q, r, ϕ and θ are considered. The RMS errors of the engine torque Q and the main rotor speed Ω are calculated separately in $J_{Q,\mathrm{RMS}}$ (scaled in %) and $J_{\Omega,\mathrm{RMS}}$ (scaled in $10 \times$ %) respectively. The corresponding RMS errors are considered as good for

$$(23a) \qquad\qquad J_{Q,\mathrm{RMS}} \leq 2$$
$$(23b) \qquad\qquad J_{\Omega,\mathrm{RMS}} \leq 2.$$

In Figure 3 on the following page the RMS error distributions of both models $\boldsymbol{G}_1$ (including Q and Ω in the model dynamics and as model output) and $\boldsymbol{G}_2$ (with Q and Ω as model outputs only) are compared as a function of the model order n. The plots show important statistical properties of the RMS errors of models with the same order n: the median of the dataset is marked in red, the minimum and maximum values in black and the upper and lower half-median in the shaded area. Thus, 50% of the RMS errors lie in the shaded range separated by the overall dataset median in red.

Both models show large RMS errors $J_\mathrm{RMS} > 2$ for low model orders $n < 20$ in Figure 3a. The RMS errors decrease significantly for increasing model order. $\boldsymbol{G}_2$ reaches a very good model accuracy with $J_\mathrm{RMS} \approx 1$ for $n \geq 70$. Model $\boldsymbol{G}_1$ achieves this accuracy level with $n \approx 95$. Thus, the torque and main rotor speed dynamics included in $\boldsymbol{G}_1$ require a higher model order to obtain the same model accuracy regarding the rigid body output RMS error in J_RMS. Most of the identified models lie in a narrow range around the median RMS error in red. Therefore, the majority of the identified models can be considered as good or very good for large model orders n.

The RMS error distributions of the engine torque Q and the main rotor speed Ω are compared for both models in Figure 3b and Figure 3c. As expected, model $\boldsymbol{G}_2$ shows considerably larger RMS errors than $\boldsymbol{G}_1$, since $\boldsymbol{G}_2$ does not include the Q and Ω dynamics. The corresponding RMS error distributions show larger maximum errors, too. Nevertheless, this effect is larger for the engine torque Q than for the

main rotor speed Ω. The RMS errors $J_{Q,\mathrm{RMS}}$ and $J_{\Omega,\mathrm{RMS}}$ do not converge as clearly to a minimum as J_RMS. Since the RMS errors of Q and Ω are quite small and constant for nearly all model orders, it is assumed that the low- and mid-frequency dynamics of Q and Ω (which have the highest contribution to the RMS error) are approximated accurately with a relative low model order. Furthermore, the model with the lowest rigid body RMS error does not necessarily provide the most accurate torque and rotor speed estimation for the evaluated parameters and model order. If J_RMS decreases below a specific limit with increasing model order, supposedly $J_{Q,\mathrm{RMS}}$ and $J_{\Omega,\mathrm{RMS}}$ will decrease further for model $\boldsymbol{G}_1$.

However, in this paper only the minimal RMS error of the rigid body outputs J_RMS according to Figure 3a is used to select the "best" models (and parameters) for $\boldsymbol{G}_1$ and $\boldsymbol{G}_2$. Information about the selected models $\boldsymbol{G}_1$ and $\boldsymbol{G}_2$ are given in Table 2.

	p	f	n	J_RMS	$J_{Q,\mathrm{RMS}}$	$J_{\Omega,\mathrm{RMS}}$
$\boldsymbol{G}_1$	225	70	118	0.92	1.34	1.09
$\boldsymbol{G}_2$	175	90	108	0.87	1.54	1.25

Table 2: Selected "best" models $\boldsymbol{G}_1$ and $\boldsymbol{G}_2$

Both models require a high past window length $p > 150$ to estimate good models. It is assumed, that the prerequisites $p > n$ and p large enough to satisfy $\boldsymbol{A}_K^p \approx \boldsymbol{0}$ are fulfilled. The future window length f is high for both models. The model order n is very high, since slow dynamics are covered by the models as well as very high frequency dynamics with $\omega > 60 \,\mathrm{rad/s}$. These dynamics cover for example vibrations resulting from the main rotor and are not needed for controller development, but are useful for high fidelity simulation. Thus, these dynamics have not been canceled using further model reduction steps. Both models provide a RMS error $J_\mathrm{RMS} < 1$, which is excellent. The RMS errors for Q and Ω are in a good range, too.

4. MODEL ANALYSIS

4.1. Model Fidelity

For a more detailed analysis of the model fidelity, the RMS errors of the eight validation maneuvers are listed separately in Table 3. In every row, the RMS errors of a validation maneuver are shown. The abbreviation in the first column gives information about the used maneuver, e.g. "$+\delta_x$" for the longitudinal cyclic validation maneuver using a positive control deflection. In the last row the overall RMS errors are summarized.

The rigid body RMS errors in J_RMS are very low for all validation maneuvers. Even though the pedal input maneuvers suffer from slightly larger RMS errors, both models are very
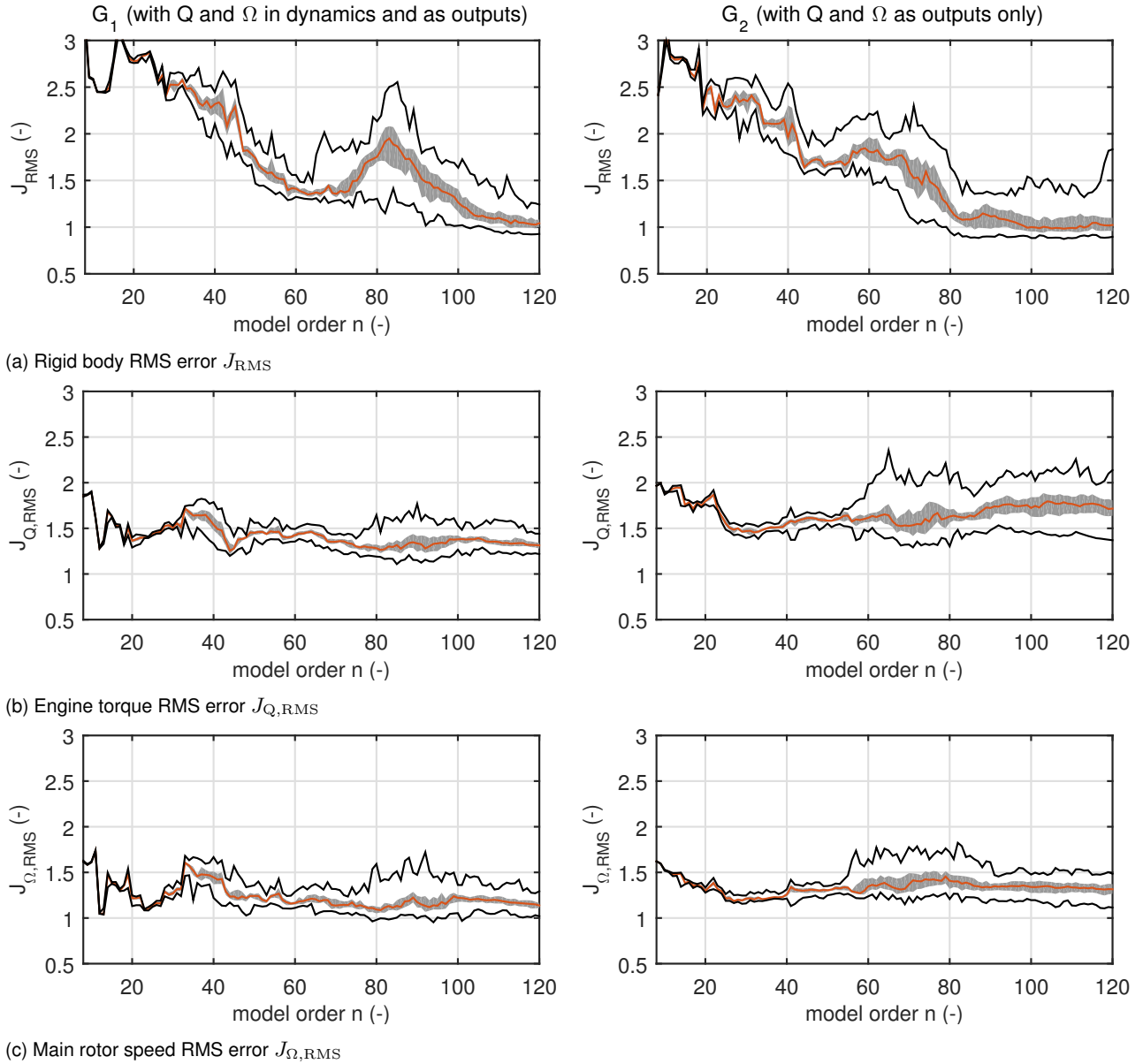
(a) Rigid body RMS error J_{RMS}

(b) Engine torque RMS error $J_{Q,\mathrm{RMS}}$

(c) Main rotor speed RMS error $J_{\Omega,\mathrm{RMS}}$

Figure 3: RMS error distribution for model $\boldsymbol{G}_1$ (left) and $\boldsymbol{G}_2$ (right) as a function of the model order n ($p \geq 50$, $f \geq 30$); median RMS error is shown in red, minimum and maximum in black, lower and upper half median shaded in gray

accurate if one takes into account that the pedal inputs are relatively large ($\pm$ 8%). In Figure 6 at the end of this paper the time domain responses of both models are compared with the corresponding measurements in the time domain for a lateral cyclic ($+\delta_y$, left plot) and a collective ($+\delta_0$, right plot) validation maneuver. A very good simulation performance regarding the rigid body outputs can be seen for both validation maneuvers. The two models are nearly congruent in the time domain plots. Since the corresponding RMS errors in Table 3 and the overall J_{RMS} are quite the same (0.92 and 0.87) this was expected beforehand.

The engine torque RMS errors $J_{Q,\mathrm{RMS}}$ and the main rotor speed RMS errors $J_{\Omega,\mathrm{RMS}}$ are good or very good ($J_{Q,\mathrm{RMS}} < 2$ and $J_{\Omega,\mathrm{RMS}} < 2$) for δ_x, δ_y and δ_0 maneu-

vers. In average, model $\boldsymbol{G}_1$ has a slightly smaller $J_{Q,\mathrm{RMS}}$ and $J_{\Omega,\mathrm{RMS}}$ than model $\boldsymbol{G}_2$, especially for "off-axis" cyclic inputs which do not change the torque and rotor speed much. This can be seen on the left side of Figure 6 for instance. The RMS errors for collective validation maneuvers are nearly the same for model $\boldsymbol{G}_1$ and $\boldsymbol{G}_2$. The shown $+\delta_0$ maneuver on the right side of Figure 6 gives the impression, that model $\boldsymbol{G}_1$ overestimates the torque and rotor speed at 4 s and is less accurate than model $\boldsymbol{G}_2$. Nevertheless, the RMS errors of the shown maneuver are comparable for both models ($J_{Q,\mathrm{RMS}}$: 1.23 and 1.31; $J_{\Omega,\mathrm{RMS}}$: 1.27 and 1.23) since $\boldsymbol{G}_1$ matches the measurement at the beginning and the end of the shown maneuver better.

For positive and negative pedal deflections, $J_{Q,\mathrm{RMS}}$ and

	J_{RMS}		$J_{Q,\mathrm{RMS}}$		$J_{\Omega,\mathrm{RMS}}$	
	$\boldsymbol{G}_1$	$\boldsymbol{G}_2$	$\boldsymbol{G}_1$	$\boldsymbol{G}_2$	$\boldsymbol{G}_1$	$\boldsymbol{G}_2$
$+\delta_x$	0.75	0.70	1.23	1.48	1.02	1.08
$-\delta_x$	0.96	0.86	1.11	0.84	0.95	0.88
$+\delta_y$	0.81	0.81	0.91	1.06	0.67	0.80
$-\delta_y$	0.76	0.67	0.72	0.81	0.55	0.61
$+\delta_p$	1.11	1.00	1.10	1.21	0.79	1.08
$-\delta_p$	1.35	1.37	2.45	3.13	2.00	2.50
$+\delta_0$	0.72	0.71	1.23	1.31	1.27	1.23
$-\delta_0$	0.71	0.61	1.31	1.17	0.83	0.83
all	0.92	0.87	1.35	1.54	1.10	1.25

Table 3: RMS errors of $\boldsymbol{G}_1$ and $\boldsymbol{G}_2$ for each validation maneuver

$J_{\Omega,\mathrm{RMS}}$ are very different, which can be seen in Table 3 as well as in Figure 7. Especially during maneuver $-\delta_p$ the measurements change heavily between 6 s and 8 s, which is not covered by any of the models. This effect is attributed to the nonlinear behavior of the fenestron tail rotor since it is observed at other airspeeds, too. Nevertheless, model $\boldsymbol{G}_1$ shows better results than $\boldsymbol{G}_2$ for pedal inputs.

In Figures 8, 9, 10 and 11 at the very end of this paper bode plots of both models are shown for all inputs to the engine torque and the main rotor speed output. The frequency response functions for the ACT/FHS generated from the manual frequency sweeps are labeled with "FR". Both models cover the low frequency dynamics ($\omega <$1 rad/s) very well for all inputs. For higher frequencies, model $\boldsymbol{G}_1$ shows significantly better approximation results using δ_x, δ_y and δ_p inputs. Since the amplitudes are quite low above 6 rad/s, this benefit of model $\boldsymbol{G}_1$ is not observable in the same manner in the time domain ($\boldsymbol{G}_1$ is better in time domain though).

The frequency responses due to collective inputs in Figure 11 show good agreement for both models, which is observed in the time domain as well. Consequently, the included torque and rotor speed dynamics in model $\boldsymbol{G}_1$ improve solely the torque and rotor speed estimation for the "off-axis" cyclic and pedal inputs. Collective inputs, which have the most influence on the torque and the rotor speed are covered very well even with the second model, which does not include torque and rotor speed dynamics. The rigid body outputs are not approximated with higher accuracy if Q and Ω are covered by the model dynamics. Therefore, it is concluded that the "major" dynamics of Q and Ω are observable in the rigid body outputs. The observable dynamics mainly have contribution to the collective input frequency responses and the low frequency dynamics of the other inputs. For an accurate approximation of the high frequency dynamics of the engine torque and main rotor speed, the corresponding outputs have to be included in the reconstruction of the system states (and thus included in the model dynamics) during system identification.

4.2. Model Structure

Linear rotorcraft or aircraft models often have a common structure which is based on physical considerations. Linear rotorcraft models include states for the rigid body motion (the velocity components, angular rates and attitude angles), rotor flapping, inflow, coning etc. depending on the complexity and the purpose of the models. Since the model states have a physical meaning, the interpretation of the eigenvalues of these models is easily obtained by analyzing the eigenvectors of the system matrix.

The identified models $\boldsymbol{G}_1$ and $\boldsymbol{G}_2$ do not have states with a physical meaning, but states which optimally solve the least squares problems in equations (14a) and (14b). Thus, the identified continuous time state space model from equation (15) has to be transformed into a representation whose structure can be interpreted. A similarity transformation is applied to the state space model by

$$(24a) \qquad \dot{\widetilde{\boldsymbol{x}}} = \boldsymbol{T}\boldsymbol{A}_{\mathrm{ct}}\boldsymbol{T}^{-1}\widetilde{\boldsymbol{x}} + \boldsymbol{T}\boldsymbol{B}_{\mathrm{ct}}\boldsymbol{u} = \widetilde{\boldsymbol{A}}_{\mathrm{ct}} + \widetilde{\boldsymbol{B}}_{\mathrm{ct}}\boldsymbol{u}$$

$$(24b) \qquad \boldsymbol{y} = \boldsymbol{C}_{\mathrm{ct}}\boldsymbol{T}^{-1}\widetilde{\boldsymbol{x}} = \widetilde{\boldsymbol{C}}_{\mathrm{ct}}\widetilde{\boldsymbol{x}}$$

with the transformed state vector $\widetilde{\boldsymbol{x}} = \boldsymbol{T}\boldsymbol{x}$ and the transformation matrix $\boldsymbol{T}$. The applied transformation is divided into two steps: In the first step, the original model is transformed into a modal canonical form with the system eigenvalues at the diagonal elements of $\boldsymbol{A}_{\mathrm{ct}}$ in increasing order (absolute values for complex eigenvalues). This is accomplished by a first transformation matrix $\boldsymbol{T}_1$. The calculation of $\boldsymbol{T}_1$ can e.g. be found in [9]. In the second step, the first n_y states (corresponding to the n_y slowest eigenvalues) of $\boldsymbol{A}_{\mathrm{ct}}$ are assigned to the model outputs $\boldsymbol{y}$ by setting up a second transformation matrix

$$(25) \qquad \boldsymbol{T}_2 = \begin{pmatrix} \boldsymbol{C}_{\mathrm{ct}}\boldsymbol{T}_1^{-1} \\ \boldsymbol{0}_{n-n_y,n} \quad \boldsymbol{I}_{n-n_y,n-n_y} \end{pmatrix}.$$

The final transformation matrix $\boldsymbol{T}$ is given by

$$(26) \qquad \boldsymbol{T} = \boldsymbol{T}_2\boldsymbol{T}_1.$$

By using this transformation, the new system states $\widetilde{\boldsymbol{x}}$ are

$$(27) \quad \widetilde{\boldsymbol{x}} = \begin{pmatrix} u & v & w & p & q & r & \phi & \theta & Q & \Omega & x_{\lambda_{n_y+1}} \dots x_{\lambda_n} \end{pmatrix}^T$$

containing the system outputs followed by the remaining modal states. The transformed output matrix $\widetilde{\boldsymbol{C}}_{\mathrm{ct}}$ is an identity matrix with $n - n_y$ zero columns. The eigenvalues and corresponding eigenvectors can be attributed to the participating rigid body and engine states using the transformed model. Since a similarity transformation does not change the eigenvalues and input-output behavior of a model, the transformed models are called $\boldsymbol{G}_1$ and $\boldsymbol{G}_2$ in this section, too.

In this section, the low- and mid-frequency ($\omega < 18$ rad/s) eigenvalues of the identified models are analyzed in detail.
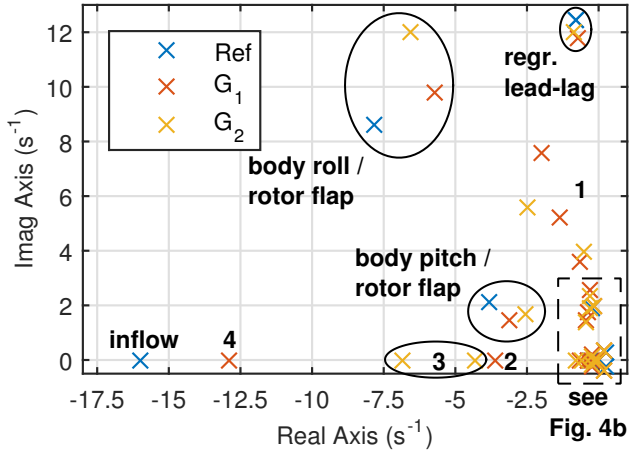
(a) Pole-zero map of eigenvalues with $\omega < 18\,\text{rad/s}$
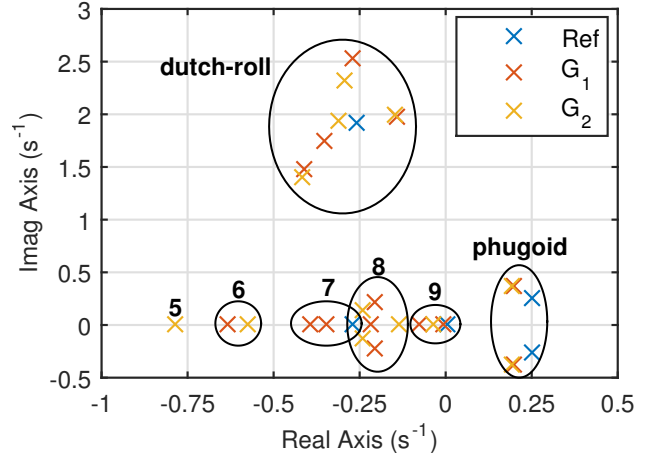
(b) Detailed view of eigenvalues in pole-zero map

Figure 4: Pole-zero map of the eigenvalues of the identified models G_1, G_2 and a reference model based on [9]

In Figure 4a the eigenvalues of both models are shown in a pole-zero map and compared to those of a 90 knots reference model containing 15 states presented in [9]. Figure 4b is a zoom-in on the low frequency eigenvalues. The eigenvalues are assigned to specific rotorcraft modes by determining the states with the highest participation in the corresponding eigenvector. Several eigenvalues cannot easily be assigned to designated rotorcraft modes, since they are highly coupled in nature. These eigenvalues are labeled with numbers in Figure 4. The modes and participating states of the corresponding eigenvector are listed in Table 4.

mode	eigenvector
regressive lead-lag	p
body-roll / rotor flap	$p\ Q$
body-pitch / rotor flap	$p\ q\ w$
inflow	w
1 coupled torque	$Q\ p$ or $Q\ r$
2 roll-yaw	$p\ r\ v$
3 torque-yaw	$Q\ r$
4 pitch-yaw	$q\ r$
phugoid	$u\ w$
dutch-roll	$v\ p\ r$
5 roll-yaw	$p\ v\ r$
6 heave-roll	$w\ p\ v$
7 heave subsidence	$w\ u$
8 coupled roll	$\phi\ u\ v\ p$
9 coupled yaw (spiral)	$\phi\ u\ r$

Table 4: System modes with corresponding eigenvectors

How the modes are characterized is shown exemplarily for the dutch-roll eigenvalues depicted in Figure 4b. Both models G_1 and G_2 have four complex poles ($\lambda_{\text{dr}1}$ to $\lambda_{\text{dr}4}$) near the reference dutch-roll eigenvalue. The largest absolute values in the corresponding eigenvectors of all four complex eigenvalues are the lateral velocity v, the roll rate p and the

yaw rate r, see Table 4. The angle from the origin to the complex number of the eigenvector in the complex plane is equal to the phase angle of the corresponding state. For the participating components these phase angles are quite similar for all four dutch-roll pole pairs, e.g. the v component with 0 deg, p between 140 deg and 170 deg and r between 265 deg and 285 deg. Furthermore, the model's responses if initialized with the corresponding eigenvector (real parts only) are evaluated in Figure 5 for model G_1 to characterize the rotorcraft modes. The initial responses of all four eigenvalues ($y_{\lambda\text{dr}1}$ to $y_{\lambda\text{dr}4}$) in Figure 5 are similar. Superposing $y_{\lambda\text{dr}1}$ to $y_{\lambda\text{dr}4}$ leads to the final dutch-roll motion $y_{\lambda\text{dr}}$ of G_1 depicted in the bottom plot of Figure 5. Thus, all four complex eigenvalues show a dutch-roll-like behavior. In their superposition, they form the dutch-roll mode of the ACT/FHS as identified with model G_1.
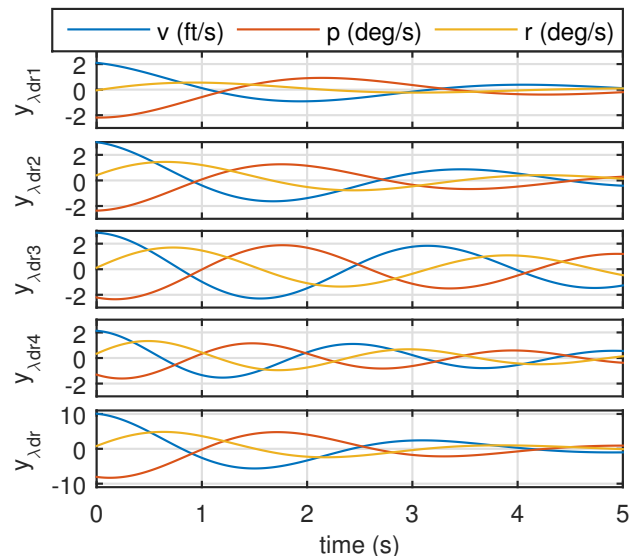

Figure 5: Initial responses of the dutch-roll eigenvalues ($y_{\lambda\text{dr}1}$ to $y_{\lambda\text{dr}4}$) and the superposed dutch-roll mode ($y_{\lambda\text{dr}}$)

In Figure 4a several eigenvalues are associated with typical rotorcraft modes. The regressive lead-lag motion is observed as a lightly damped oscillation of the roll rate p at about 12 rad/s. A coupled motion between the roll rate p and torque Q can be found between 11.3 rad/s and 13.7 rad/s. This mode is called body roll / rotor flap in [9]. The body pitch / rotor flap mode is observed between 3 rad/s and 3.5 rad/s. This mode involves a coupled roll, pitch and heave motion. Even if the models G_1 and G_2 do not provide exactly the same eigenvalues, the corresponding frequencies and damping factors of the eigenvalues are comparable. Furthermore, the shown eigenvalues involve the same rotorcraft states and can be found in the reference model as well. Several eigenvalues with coupled torque, roll and yaw motions can be found in model G_1 and G_2 for mode "1", but not in the reference model. Model G_1 has three complex eigenvalues in mode "1", model G_2 just two. But model G_2 contains two further real eigenvalues labeled as mode "3" with high torque participation and nearly the same frequency of the eigenvalues as in mode "1". The inflow mode of the reference model cannot be found in G_1 or G_2. This is due to the fact that the inflow mode of the reference model is a simplified characterization of the coupled inflow / coning dynamics.

The models G_1 and G_2 have many low frequency eigenvalues shown in Figure 4b. The unstable phugoid eigenvalues can be found at $0.19 \pm i0.37$. The phugoid eigenvalues of G_1 and G_2 are nearly congruent, but slightly different from the reference model's. The characterization of the dutch-roll was described before. The coupled yaw mode "9" includes ϕ, u and r, thus it seems to be the spiral mode as the reference model has the spiral mode in this area, too. Nevertheless, the proximity of these low frequency eigenvalues hinders a more specific classification. Probability some of the shown eigenvalues have to be superposed like the dutch-roll eigenvalues to result in a specific rotorcraft mode.

In summary, the low frequency eigenvalues are mainly influenced by the rigid body states of the helicopter. With increasing frequency, the helicopter engine and rotor states have a more significant influence on the eigenvalues of both models. These results support the evaluation in section 4.1. The rigid body states are accurate for both models and the corresponding eigenvalues are comparable. The so-called "major" dynamics of Q and Ω are observable through the rigid body responses. The body-roll / rotor-flap mode shows a large influence of Q for both models and this mode can be found in the reference model which is identified without engine and rotor speed dynamics for instance. Furthermore, the models G_1 and G_2 have several lightly damped eigenvalues between 4 rad/s and 8 rad/s (mode "1" in Figure 4a) with a main contribution of the engine torque, even if G_2 has no torque included in its dynamics. Nevertheless, for higher frequencies above 30 rad/s the eigenvalues of both models differ profoundly from each other with the exception of some characteristic resonances of the rotorcraft. For

an appropriate approximation of the high frequency torque and main rotor speed dynamics, these outputs have to be included in the model dynamics estimation step. Additionally, it is assumed that further rotor states participate in the eigenvalues with increasing frequency. Since the ACT/FHS is not yet equipped with a full rotor measuring system, these states cannot be separated further in this paper.

5. CONCLUSIONS AND OUTLOOK

Two models of the ACT/FHS rotorcraft have been identified applying the PBSIDopt method to flight test data to determine the influence of the engine torque and the main rotor speed on model fidelity and model structure. The first model includes the rigid body states as well as the engine torque and the main rotor speed in the model dynamics and outputs. The dynamics of the second model are based on the rigid body states only. Engine torque and main rotor speed are included in the second model just as additional outputs for the comparison with the first model. Both models have been compared in detail:

- Both models require a large model order $n > 100$ to provide excellent simulation results with $J_{\mathrm{RMS}} < 1$,
- Model 1 requires slightly more states to achieve the same accuracy as model 2,
- Model 1 covers the engine torque and main rotor speed more precisely than model 2,
- Torque and rotor speed responses due to collective inputs are accurate for both models,
- The analyzed eigenvalues of both models are comparable and can be attributed to common rotorcraft modes,
- The eigenvalues of model 2 show a comparable participation of the engine torque as model 1, even if torque is only considered as additional output.

Thus, the overall model fidelity regarding solely the rigid body states is not dependent on the engine torque and main rotor speed, since both models provide very accurate estimation of the rigid body states. The engine torque and main rotor speed is accurate for both models regarding collective inputs or the low frequency dynamics only. It is thus concluded, that these "major" dynamics are observable through the rigid body states. Therefore, it should be possible to identify these dynamics with the classical Maximum Likelihood method using only the rigid body states, too. Nevertheless, the high frequency dynamics and "off-axis" responses due to cyclic or pedal inputs for engine torque and main rotor speed are covered merely by the first model.

In the next step, the high order models should be reduced to a low order representation for the usage in flight control development for the ACT/FHS. The analysis of the model structure should be simplified using reduced models, too.

REFERENCES

[1] Tischler, M. B. and Remple, R. K., *Aircraft and Rotorcraft System Identification: Engineering Methods with Flight-Test Examples*, American Institute of Aeronautics and Astronautics, Inc., Reston, Virginia, USA, 2nd ed., 2012.

[2] Lantzsch, R., Greiser, S., Wolfram, J., Wartmann, J., Müllhäuser, M., Lüken, T., Döhler, H.-U., and Peinecke, N., "ALLFlight: A Full Scale Pilot Assistance Test Environment," *American Helicopter Society 68th Annual Forum*, Forth Worth, Texas, USA, 2012.

[3] Greiser, S., Lantzsch, R., Wolfram, J., Wartmann, J., Müllhäuser, M., Lüken, T., Döhler, H.-U., and Peinecke, N., "Results of the pilot assistance system "Assisted Low-Level Flight and Landing on Unprepared Landing Sites" obtained with the ACT/FHS research rotorcraft," *Aerospace Science and Technology*, Vol. 45, Sept. 2015, pp. 215–227. doi:10.1016/j.ast.2015.05.017.

[4] Seher-Weiss, S. and von Grünhagen, W., "EC135 System Identification for Model Following Control and Turbulence Modeling," *Proceedings of the 1st CEAS European Air and Space Conference*, Sept. 2007, pp. 2439–2447.

[5] Seher-Weiss, S. and von Gruenhagen, W., "Development of EC 135 turbulence models via system identification," *Aerospace Science and Technology*, Vol. 23, No. 1, Dec. 2012, pp. 43–52. doi:10.1016/j.ast.2011.09.008.

[6] Seher-Weiss, S. and von Grünhagen, W., "Comparing explicit and implicit modeling of rotor flapping dynamics for the EC 135," *CEAS Aeronautical Journal*, Vol. 5, No. 3, Sept. 2014, pp. 319–332. doi:10.1007/s13272-014-0109-0.

[7] Seher-Weiss, S., "Comparing different approaches for modeling the vertical motion of the EC 135," *accepted for publication in CEAS Aeronautical Journal*, Feb. 2015. doi:10.1007/s13272-015-0150-7.

[8] Greiser, S. and von Grünhagen, W., "Analysis of Model Uncertainties Using Inverse Simulation," *American Helicopter Society 69th Annual Forum*, Phoenix, Arizona, USA, 2013.

[9] Greiser, S. and Seher-Weiss, S., "A contribution to the development of a full flight envelope quasi-nonlinear helicopter simulation," *CEAS Aeronautical Journal*, Vol. 5, No. 1, March 2014, pp. 53–66. doi:10.1007/s13272-013-0090-z.

[10] Wartmann, J., "Model validation and analysis using feedforward control flight test data," *accepted for publication in CEAS Aeronautical Journal*, March 2015. doi:10.1007/s13272-015-0152-5.

[11] Chiuso, A., "The role of vector autoregressive modeling in predictor-based subspace identification," *Automatica*, Vol. 43, No. 6, June 2007, pp. 1034–1048. doi:10.1016/j.automatica.2006.12.009.

[12] Chiuso, A., "On the Asymptotic Properties of Closed-Loop CCA-Type Subspace Algorithms: Equivalence Results and Role of the Future Horizon," *IEEE Transactions on Automatic Control*, Vol. 55, No. 3, 2010, pp. 634–649.

[13] Li, P. and Postlethwaite, I., "Subspace and Bootstrap-Based Techniques for Helicopter Model Identification," *Journal of the American Helicopter Society*, Vol. 56, No. 1, 2011. doi:10.4050/JAHS.56.012002.

[14] Bergamasco, M. and Lovera, M., "Continuous-Time Predictor-Based Subspace Identification For Helicopter Dynamics," *37th European Rotorcraft Forum*, Milano, Italy, 2011.

[15] Sguanci, M., Bergamasco, M., and Lovera, M., "Continuous-Time Model Identification for Rotorcraft Dynamics," *16th IFAC Symposium on System Identification*, Brussels, Belgium, 2012.

[16] Wartmann, J. and Seher-Weiss, S., "Application of the Predictor-Based Subspace Identification Method to Rotorcraft System Identification," *39th European Rotorcraft Forum*, Moscow, Russia, 2013.

[17] Kaletka, J., Kurscheid, H., and Butter, U., "FHS, the New Research Helicopter: Ready for Service," *Aerospace Science and Technology*, Vol. 9, No. 5, July 2005, pp. 456–467.

[18] Wartmann, J., Wolfram, J., and Gestwa, M., "Sensor Fusion and Flight Path Reconstruction of the ACT/FHS Rotorcraft," *Deutscher Luft- und Raumfahrtkongress*, Augsburg, Germany, 2014.

[19] Särkkä, S., "Unscented Rauch-Tung-Striebel Smoother," *IEEE Transactions on Automatic Control*, Vol. 53, No. 3, April 2008.
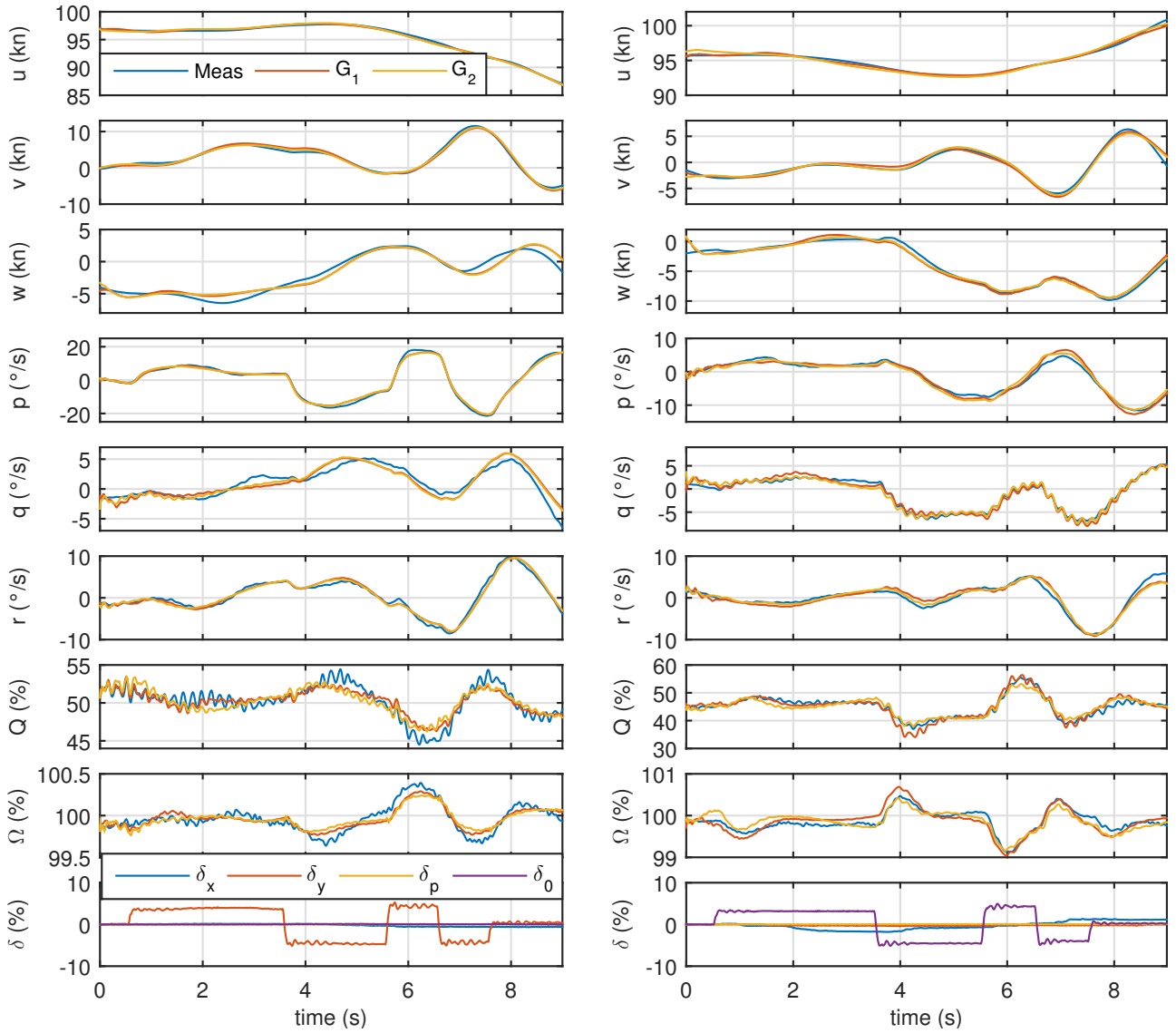
Figure 6: Time domain responses of ACT/FHS models G_1 and G_2, maneuver $+\delta_y$ (left side) and $+\delta_0$ (right side) (90 knots)
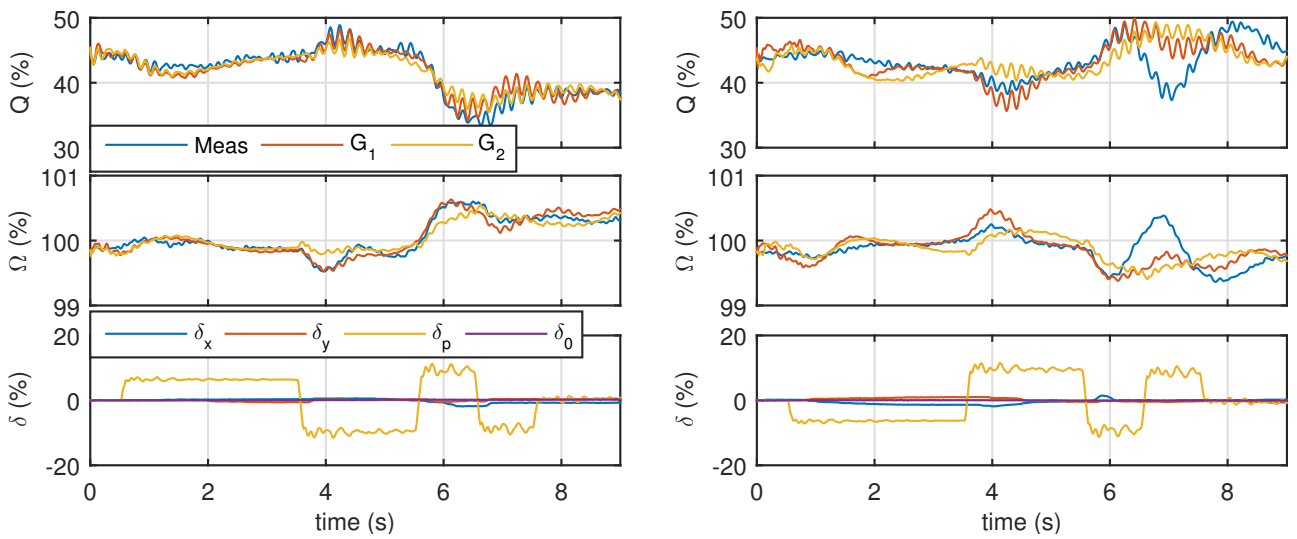

Figure 7: Q and Ω responses of ACT/FHS models G_1 and G_2, maneuver $+\delta_p$ (left side) and $-\delta_p$ (right side) (90 knots)
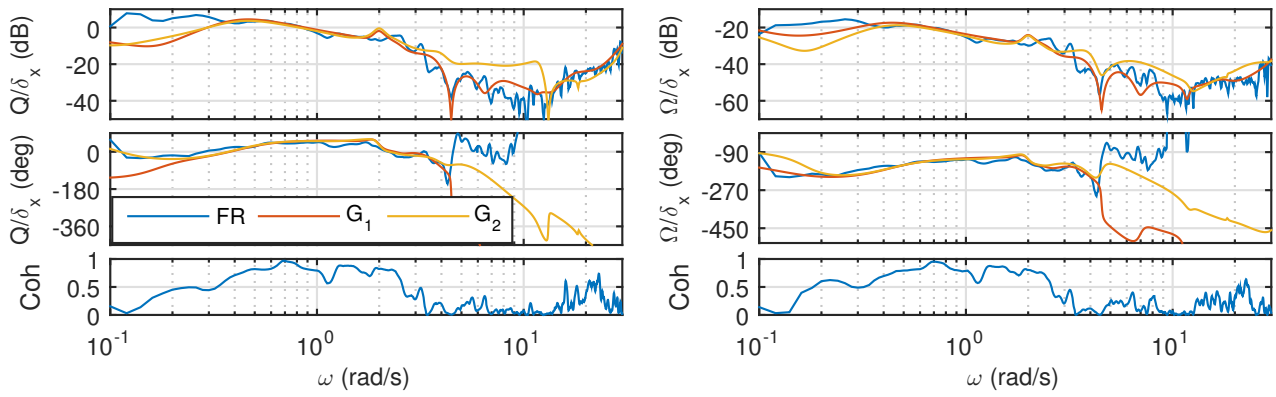
Figure 8: Bode plots of engine torque Q (left) and main rotor speed Ω (right) due to longitudinal cyclic inputs (90 knots)
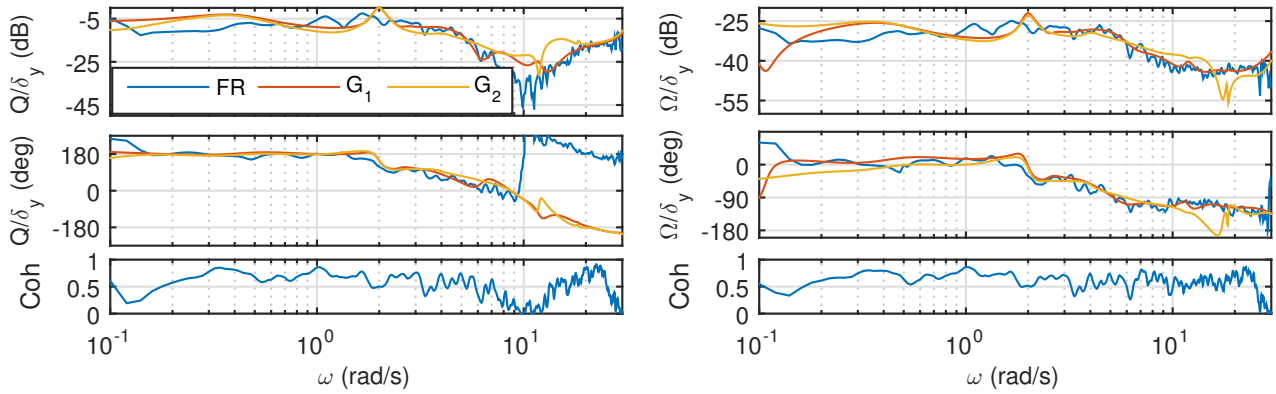

Figure 9: Bode plots of engine torque Q (left) and main rotor speed Ω (right) due to lateral cyclic inputs (90 knots)
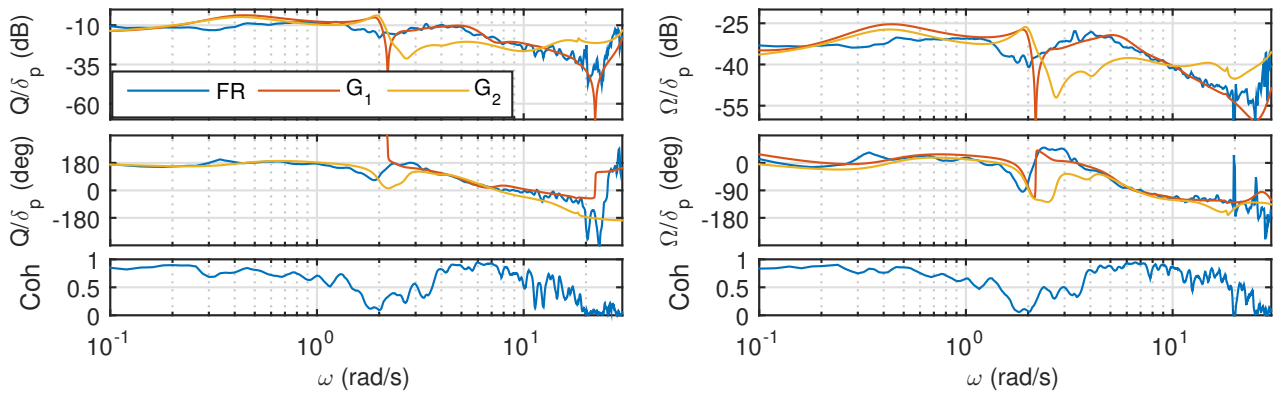

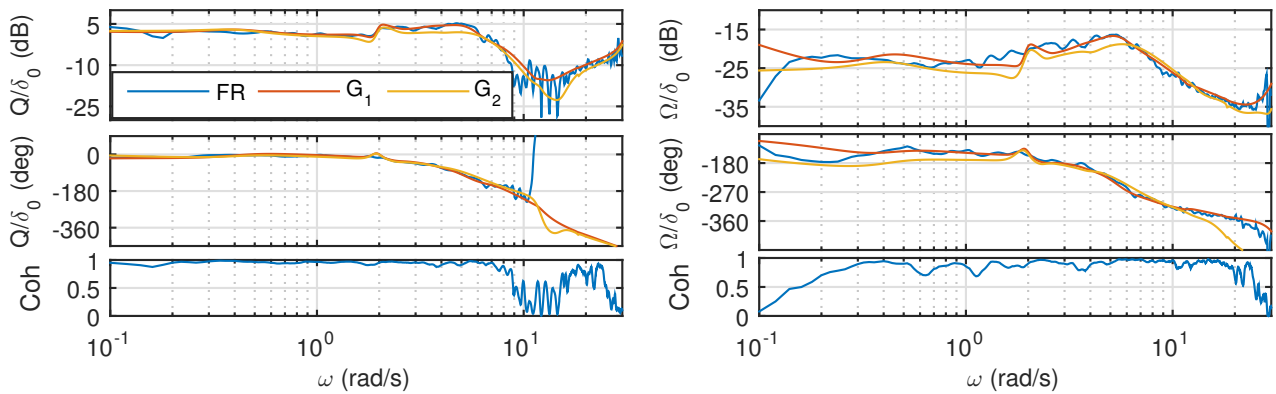Figure 10: Bode plots of engine torque Q (left) and main rotor speed Ω (right) due to pedal inputs (90 knots)

Figure 11: Bode plots of engine torque Q (left) and main rotor speed Ω (right) due to collective inputs (90 knots)